MNRAS **000**, 1–14 (2017) Preprint 5 February 2018 Compiled using MNRAS LATEX style file v3.0

Kinetic-MHD simulations of gyroresonance instability driven by CR pressure anisotropy

O. Lebiga,[1,2,3]⋆ R. Santos-Lima,[1,2]† H. Yan,[1,2]‡
[1] *DESY, Platanenallee 6, 15738 Zeuthen, Germany*
[2] *Institut für Physik und Astronomie, Universität Potsdam, 14476 Potsdam-Golm, Germany*
[3] *Taras Shevchenko National University of Kyiv, 64/13, Volodymyrska Street, Kyiv, Ukraine, 01601*

5 February 2018

ABSTRACT

The transport of cosmic rays (CRs) is crucial for the understanding of almost all high-energy phenomena. Both pre-existing large-scale magnetohydrodynamic (MHD) turbulence and locally generated turbulence through plasma instabilities are important for the CR propagation in astrophysical media. The potential role of the resonant instability triggered by CR pressure anisotropy to regulate the parallel spatial diffusion of low-energy CRs ($\lesssim$ 100 GeV) in the interstellar and intracluster medium of galaxies (ISM and ICM) has been showed in previous theoretical works. This work aims to study the gyroresonance instability via direct numerical simulations, in order to access quantitatively the wave-particle scattering rates. For this we employ a 1D PIC-MHD code to follow the growth and saturation of the gyroresonance instability. We extract from the simulations the pitch-angle diffusion coefficient $D_{\mu\mu}$ produced by the instability during the linear and saturation phases, and a very good agreement (within a factor of 3) is found with the values predicted by the quasilinear theory (QLT). Our results support the applicability of the QLT for modeling the scattering of low-energy CRs by the gyroresonance instability in the complex interplay between this instability and the large-scale MHD turbulence.

Key words: cosmic ray – *(magnetohydrodynamics)* MHD – turbulence – plasmas

1 INTRODUCTION

Basic processes of transport of cosmic rays (CRs) are crucial for understanding most of high-energy phenomena, ranging from solar flares (Yan et al. 2008), γ-ray emission of molecular clouds associated to supernova remnants (Nava & Gabici 2013), to remote cosmological objects such as γ-ray bursts (Zhang & Yan 2011). The interaction of CRs with magnetohydrodynamic (MHD) turbulence is thought to be the principal mechanism to scatter and isotropize CRs (e.g. Ginzburg 1966; Jokipii 1966; Wentzel 1969; Schlickeiser 2002; Yan 2015 and ref. therein). In addition to the large-scale MHD turbulence, small-scale instability generated perturbations also play crucial roles. In the context of acceleration in supernova shocks, studies of instabilities have been one of the major efforts in the field since the acceleration efficiency is essentially determined by the confinement at the shock region and magnetic field amplification (e.g. Bell & Lucek 2001; Bell 2004; Yan et al. 2012; Caprioli & Spitkovsky 2014; Brose, Telezhinsky, & Pohl 2016).

The diffusive propagation of CRs in the Galaxy, far from sources, is considered to be regulated by the interactions with the interstellar medium (ISM) background turbulence. However, due to the damping of the background turbulence (particularly the fast modes), CRs with energies below $\sim$ 100 GeV are expected to be mainly influenced by the self-generated instabilities. In fact, the small-scale instabilities and large-scale turbulence are not independent of each other. First, the instability generated waves can be damped through the interaction with the large-scale turbulence (Yan & Lazarian 2002; Farmer & Goldreich 2004; Lazarian 2016). Second, the large-scale compressible turbulence also generate small-scale waves through thermal plasma (e.g. Schekochihin et al. 2005; Santos-Lima et al. 2014, 2016; Sironi & Narayan 2015) and CR resonant instabilities (Lazarian & Beresnyak 2006; Yan & Lazarian 2011).

The compression/expansion and shear from the large-scale ISM turbulence produce deformations in the local particle pitch angle distribution due to the conservation of the first adiabatic invariant. Such anisotropic distributions are subjected to various instabilities. Waves

⋆ Contact e-mail: olga.lebiga@desy.de
† Contact e-mail: reinaldo.santos.de.lima@desy.de
‡ Contact e-mail: huirong.yan@desy.de

generated through instabilities enhance the scattering rates of the particles, and their distribution then relaxed to the state of marginal state of instability even in the collisionless environment (Schekochihin & Cowley 2006; Kunz, Schekochihin, & Stone 2014; Santos-Lima et al. 2016; Sironi & Narayan 2015; Riquelme, Quataert, & Verscharen 2015). In particular, the anisotropy in the CR pressure induces a (gyro)resonant instability. Unlike the streaming instability (e.g. Skilling 1970, 1971, 1975; Amato & Blasi 2009), this gyroresonance instability does not require the bulk motion of CRs. The wave grows at the expense of the free energy from CRs' anisotropy induced by the large-scale turbulent motions. In the case that the energy growth rate reaches the turbulence energy cascading rate, turbulence is damped (Yan & Lazarian 2011). This is one of the feedbacks from CRs on turbulence.

Yan & Lazarian (2011, YL11 hereafter) proposed an analytical equilibrium model of the CR diffusion resulting from their scattering by the gyroresonance instability, based on the quasilinear theory (QLT). They derived the dependence of the diffusion coefficients with the parameters of the medium turbulence, taking into accout self-consistently the damping effect of the instability on the large-scale compressible cascade. They found this mechanism to be important for the CR propagation in collisionless medium, such as the Halo and hot ionized medium of the Galaxy, and also in the intracluster medium (ICM) of galaxies.

These previous findings motivate more detailed studies on this scattering mechanism and its role in the CR propagation in both the ISM and ICM. The saturation state of the instability as well as the accuracy of the CR scattering rates based on the QLT are addressed in this work. For this aim, we use direct numerical simulations to follow the evolution of an initially unstable CR distribution propagating in a thermal background plasma. These simulations are based on a hybrid technique which combines Particle-In-Cell (PIC) and MHD (e.g. Lucek & Bell 2000; Bai et al. 2015). This first study is restricted to unidirectional propagating modes, parallel to the mean field (one-dimensional geometry).

This paper is organized in the following way: in §2 we present the basic equations which describe the relevant CR interactions with the background thermal plasma, the dispersion relation for the transverse modes propagating parallel to the magnetic field for a distribution of CRs with pressure anisotropy, and the QLT prediction for the CR pitch-angle diffusion coefficient. In §3 we describe the numerical methods employed in our numerical simulations, and the results are presented in §4. Finally, in §5 we summarize our findings and offer our conclusions.

2 CR PRESSURE ANISOTROPY GYRORESONANCE INSTABILITY

2.1 CR + thermal plasma description

The relevant physical phenomena for the CR propagation (considered only as ions here) in the ISM or ICM take place on scales larger or of the order of the CR kinetic scales, many orders of magnitude above the kinetic scales of the thermal ions in the medium. Hence for studying the effects of the interactions between CRs and the thermal plasma it is natural to retain the kinetic description only for the CRs, employing the Vlasov equation for the evolution of their distribution function $f(\mathbf{r},\mathbf{p},t)$:

$$\frac{\partial f}{\partial t}+\mathbf{v}\cdot\frac{\partial f}{\partial \mathbf{r}}+q\left(\mathbf{E}+\frac{1}{c}\mathbf{v}\times\mathbf{B}\right)\cdot\frac{\partial f}{\partial \mathbf{p}}=0, \tag{1}$$

where $\mathbf{v}=\mathbf{p}/\gamma m_{cr}$ is the CR velocity, $\gamma=\left(1-v^2/c^2\right)^{-1/2}$, c is the light speed, m_{cr} is the CR rest mass, q is the CR charge (elementary charge e in our case), $\mathbf{E}$ and $\mathbf{B}$ are the electric and magnetic fields. The mass-dominating thermal plasma is described by the MHD approximation, modified to account for the CRs presence:

$$\frac{\partial \rho}{\partial t}+\nabla\cdot(\rho\mathbf{u})=0, \tag{2}$$

$$\rho\left[\frac{\partial \mathbf{u}}{\partial t}+(\mathbf{u}\cdot\nabla)\mathbf{u}\right]+ \\ +\nabla P_{th}-\frac{1}{4\pi}(\nabla\times\mathbf{B})\times\mathbf{B}=-\frac{1}{c}\mathbf{J}_{cr}\times\mathbf{B}-qn_{cr}\mathbf{E}, \tag{3}$$

$$\frac{\partial \mathbf{B}}{\partial t}=-c\nabla\times\mathbf{E}, \tag{4}$$

$$\nabla\times\mathbf{B}=\frac{4\pi}{c}\left(\mathbf{J}_{th}+\mathbf{J}_{cr}\right),\quad \nabla\cdot\mathbf{B}=0, \tag{5}$$

where ρ, $\mathbf{u}$, P_{th}, $\mathbf{J}_{th}$ are the density, velocity, thermal pressure, and current density fields of the thermal plasma, n_{cr} and $\mathbf{J}_{cr}$ are the number and current density of the CRs:

$$n_{cr}(\mathbf{r},t)=\int d\mathbf{p}\; f(\mathbf{r},\mathbf{v},t), \tag{6}$$

$$\mathbf{J}_{cr}(\mathbf{r},t)=q\int d\mathbf{p}\;\mathbf{v}f(\mathbf{r},\mathbf{v},t). \tag{7}$$

in the ideal case when the resistivity can be neglected, the electric field is given by:

$$\mathbf{E}=-\frac{1}{c}\mathbf{u}\times\mathbf{B}. \tag{8}$$

The above equations (Bykov et al. 2013) assume (i) the thermal plasma is non-relativistic, and (ii) quasi-neutrality of the full plasma: $q_i n_i + qn_{cr} = en_e$, where $n_{i,e}$ is the number density of the thermal ions/electrons, q_i is the ions charge, and e is the elementary charge. For simplicity, we consider the thermal plasma composed only by protons and electrons, and the CRs as protons ($q = q_i = e$, $m_{cr} = m_i = m_p$, where m_p is the proton mass). The system must be closed by an equation for the evolution of P_{th}.

2.2 Development of CR pressure anisotropy

The momentum distribution of CRs propagating in a region where the local magnetic field intensity B is changing slowly in time (compared to the CR gyroperiod) becomes distorted as the perpendicular component of the particles momentum $p_\perp$ modifies according to the conservation of the first adiabatic invariant $\propto p_\perp^2/B$ (e.g. Longair 2011). In this way an initially isotropic distribution function $f_0(\mathbf{p})d\mathbf{p}\propto p^{-2-\alpha}d\mathbf{p}$ assumes an elliptic shape in the momentum space:

$$f(\mathbf{p})d\mathbf{p}\propto\left(\xi p_\perp^2+p_\parallel^2\right)^{-1-\alpha/2}d\mathbf{p}, \tag{9}$$

where $\parallel, \perp$ refer to the directions parallel/perpendicular to the local magnetic field $\mathbf{B}$. In general, we can parametrize small deviations from the isotropy by using an expansion in the distribution of the cosine of the pitch-angle $\mu = p_\parallel/|\mathbf{p}|$:

$$\begin{aligned} &f(\mathbf{p})d\mathbf{p} = N(p)p^2 dp g(\mu) d\mu d\psi, \\ &g(\mu) \propto 1 + 3\beta\mu + \frac{\chi}{2}\left(3\mu^2 - 1\right), \end{aligned} \tag{10}$$

where ψ is the gyro-phase and $|\beta|, |\chi| \ll 1$. The above distribution is obviously restricted to the case of uniform anisotropy over all p. In this study we neglect the dipole component β (no CR bulk velocity). In this case, the above distribution function translates in an anisotropy A of the CR pressure components $P_{\perp,\parallel}$ defined by

$$A \equiv P_\perp/P_\parallel - 1, \tag{11}$$

where

$$P_\perp \equiv \frac{1}{2}\int d\mathbf{p} f(\mathbf{p}) v_\perp p_\perp, \quad P_\parallel \equiv \int d\mathbf{p} f(\mathbf{p}) v_\parallel p_\parallel. \tag{12}$$

The correspondence between χ and A is

$$\chi = \frac{5A}{2A+3} = \frac{5}{3}A + \mathcal{O}\left(A^2\right). \tag{13}$$

The analytical model in YL11 provides the following estimates for A: $\gtrsim 10^{-3}$ for the galactic Halo and $\gtrsim 10^{-4}$ for the hot interstellar medium and ICM. Although this work is dedicated to study the isolated effects of CR pressure anisotropy, it should be observed that we expect a large scale drift of CRs flowing from the galactic sources to outside the Galaxy, with this dipole anisotropy (of the order of β) observed to be $10^{-4} - 10^{-3}$ at the Earth (Skilling 1970; Di Sciascio & Iuppa 2014). A systematic study on the combined effect of both kinds of anisotropy is beyond the scope of the present work, and will be addressed elsewhere.

2.3 Parallel propagating transverse modes

The dispersion relation of the ordinary linear MHD waves can be modified depending on the CRs distribution function. In fact the free-energy provided by the anisotropic pressure of CRs can turn the MHD waves unstable (e.g. Schlickeiser 2002). We focus here only on the parallel propagating modes, for simplicity and also because they have the fastest growth rates, and therefore should be more important for CR scattering. Bykov et al. (2013) present the linear dispersion relation for the general case of a distribution function described by Eq. 10. In the absense of CR bulk velocity ($\beta = 0$), the linear dispersion relation for $k > 0$ is [1]:

$$\omega^2 = v_A^2\left\{k^2 \mp k\frac{4\pi q n_{cr}\chi}{B_0}\int_{p_{\min}}^{p_{\max}}\sigma(p,k)N(p)p^2dp\right\}, \tag{14}$$

where we assume $|\omega| \ll |\Omega|$, $\Omega = \Omega_0/\gamma$ is the CR cyclotron frequency with $\Omega_0 = qB_0/m_{cr}c$, $v_A = B_0/\sqrt{4\pi\rho}$ is the Alfvén speed, $p_{\min}$ and $p_{\max}$ are the minimum and maximum values of the CR momentum distribution $N(p)$, and

$$\sigma(p,k) = \frac{3}{4}\int_{-1}^{1}\frac{(1-\mu^2)\mu}{1 \mp kv\mu/\Omega}d\mu, \tag{15}$$

[1] The solution in Eq. 14 is rigorously derived for $\mathrm{Im}(\omega) > 0$. The validity of this expression for $\mathrm{Im}(\omega) < 0$ comes from the analytical continuation of the solution.

where $\mp$ correspond to the Left and Right circular polarization, respectively. We adopt the definition of polarization used in Stix (1962) and Gary (1993): the waves with Left polarization rotate in the same sense as protons, irrespective to the wave propagation direction, while the waves with Right polarization rotate with the same sense as electrons.

According to the dispersion relation given by Eq. 14, for small anisotropies ($|\chi| \ll 1$) the real (ω_r) and imaginary (Γ) parts of the frequency are:

$$|\omega_r(k)| = v_A k + \mathcal{O}(\chi), \tag{16}$$

$$\Gamma^{L,R}(k) = \mp v_A\frac{2\pi q n_{cr}\chi}{B_0}\,\mathrm{Im}\left\{\int_{p_{\min}}^{p_{\max}}\sigma(p,k)N(p)p^2dp\right\} + \\ + \mathcal{O}(\chi^2). \tag{17}$$

Using the analytical solution in Bykov et al. (2013), the imaginary part in $\sigma(p,k)$ (Eq. 15) comes from the pole (resonant) contribution and is given by:

$$\mathrm{Im}\left\{\sigma(p,k)\right\} = -\frac{3\pi}{4}\left[\left(\frac{\Omega_0 m_{cr}}{kp}\right)^2 - \left(\frac{\Omega_0 m_{cr}}{kp}\right)^4\right]\times \\ \times\,\mathcal{H}\left(p - m_{cr}\Omega_0/k\right) \tag{18}$$

where $\mathcal{H}(x)$ is the Heaviside step function. Assuming the following power law for the momentum distribution:

$$N(p) = \frac{(1-\alpha)}{\left(p_{\max}^{1-\alpha} - p_{\min}^{1-\alpha}\right)}p^{-2-\alpha} \tag{19}$$

for $p_{\min} < p < p_{\max}$ and zero otherwise, the integration in Eq. 17 gives:

$$\mathrm{Im}\left\{\int_{p_{\min}}^{p_{\max}}\sigma(p,k)N(p)p^2dp\right\}(k) \approx \\ \approx -\frac{3\pi}{4}\frac{(\alpha-1)}{(\alpha+1)}\times\begin{cases} 0, & \text{if } kr_{\min} < p_{\min}/p_{\max} \\ (kr_{\min})^{\alpha-1}, & \text{if } p_{\min}/p_{\max} < kr_{\min} < 1 \\ (kr_{\min})^{-2}, & \text{if } kr_{\min} > 1 \end{cases} \tag{20}$$

where $r_{\min} \equiv p_{\min}/m_{cr}\Omega_0$ is the Larmor radius for the lower energy particles (in the limit of zero pitch-angle), and assuming $\alpha > 2$, $p_{\max}/p_{\min} \gg 1$. Now we can rewrite Eq. 17 as:

$$\Gamma^{L,R}(k) \approx \pm\frac{5\pi}{8}\frac{(\alpha-1)}{(\alpha+1)}\left(\frac{c}{v_A}\right)\Omega_0\left(\frac{n_{cr}}{n_i}\right)A\times \\ \times\begin{cases} 0, & \text{if } kr_{\min} < p_{\min}/p_{\max} \\ (kr_{\min})^{\alpha-1}, & \text{if } p_{\min}/p_{\max} < kr_{\min} < 1 \\ (kr_{\min})^{-2}, & \text{if } kr_{\min} > 1. \end{cases} \tag{21}$$

2.4 Quasilinear instability evolution

The parallel propagating Alfvén waves with polarization L (if $A > 0$) or R (if $A < 0$) grow exponentially and scatter resonantly the CRs. This scattering can be described by a pitch-angle diffusion coefficient in the Fokker-Planck equation for the evolution of the ensemble averaged distribution function $\langle f(\mathbf{r},\mathbf{p},t)\rangle$:

$$\left(\frac{\partial\langle f\rangle}{\partial t}\right)_{scatt} = \frac{\partial}{\partial\mu}\left(D_{\mu\mu}\frac{\partial\langle f\rangle}{\partial\mu}\right). \tag{22}$$

The dependence of the diffusion coefficient $D_{\mu\mu}$ with the electromagnetic waves properties (dispersion and amplitude) can be derived analytically under the quasilinear theory, valid for small amplitude random-phased waves. In Appendix A we present a derivation of $D_{\mu\mu}$ using a procedure equivalent to the quasilinear theory. Under the set of hypothesis detailed in the Appendix and observing that the real frequency of the waves L and R are almost identical, i.e. $\omega^L_{r,n}(k) \approx \omega^R_{r,n}(k) = \omega_r(k)$ ($n = f, b$ for forward or backward propagation directions, respectively), we obtain:

$$D^{QL}_{\mu\mu}(\delta t) = \frac{\Omega^2(1-\mu^2)}{2}\int_0^\infty dk \frac{|\mathbf{B}(k)|^2}{B_0^2}\times \\ \times\left\{[1+\sigma_H(k)]\mathcal{R}(v\mu k - \omega_r + \Omega, \delta t) + \right. \\ \left. [1-\sigma_H(k)]\mathcal{R}(v\mu k - \omega_r - \Omega, \delta t)\right\}, \quad (23)$$

where the resonance function $\mathcal{R}$ is given by Eq. A20, $\sigma_H(k)$ is the total helicity of the waves component of $\mathbf{B}(k)$. $\sigma_H = -1$ for waves with L polarization and forward propagation or R polarization and backward propagation; $\sigma_H = +1$ for L polarization and backward propagation or R polarization and forward propagation. The time interval δt is understood as the time interval under which the diffusion process is considered, and it is much shorter than the timescale of change of the distribution function due to the scattering itself (see Appendix A). Therefore, the above definition of the diffusion coefficient is valid for describing the evolution of distribution functions averaged in a time interval $\sim \delta t$. Because the system we are focusing in this study is statistically homogeneous and the theoretical $D^{QL}_{\mu\mu}$ does not depend on the gyro-phase, we can consider the average of the Fokker-Planck equation in space and gyro-phase.

The effect of $D_{\mu\mu}$ is to reduce gradually the anisotropies in μ of the distribution function: the source of free-energy of the instability. Therefore after the linear phase, the initial distribution function of the CRs will evolve reducing the μ anisotropy, then reducing the instability growth rate. During this last saturation phase, the distribution function will gradually relax to a stable distribution (isotropic). The diffusion timescale depends on Ω, or on the particle energy. This means that the anisotropy distribution over p does not evolve uniformly, i.e. $A = A(p)$ after the linear phase.

The CR mean-free-path along the field lines (from the scattering of particles along this direction) is related to $D_{\mu\mu}$ via:

$$\lambda_\parallel = \frac{3}{4}v\int_{-1}^{1} d\mu \frac{(1-\mu^2)}{\nu_{scatt}} = \frac{3}{8}v\int_{-1}^{1} d\mu \frac{(1-\mu^2)^2}{D_{\mu\mu}}, \quad (24)$$

where $\nu_{scatt} \equiv 2D_{\mu\mu}/(1-\mu^2)$ is the CR scattering rate.

3 NUMERICAL METHODS

In order to study the evolution of the CR pressure anisotropy instability described by the MHD + CR kinetic equations (see §2.1), we use an hybrid MHD-particle code which represents the MHD fields (ρ, $\mathbf{u}$, P_{th}, $\mathbf{B}$) in cells defined by a grid over the simulation domain, while the CR distribution function is sampled by a collection of macro-particles which orbits are directly solved. The CR macroscopic fields needed for the evolution of the MHD variables ($n_{cr}, \mathbf{J}_{cr}, \mathbf{u}_{cr}$) are calculated by a process of deposition of the macro-particles on the grid cells (Particle-In-Cell method). This MHD-PIC coupling is described in detail in Bai et al. (2015).

The grid cell variables are evolved by the following set of equations:

$$\frac{\partial \rho}{\partial t} + \nabla\cdot(\rho\mathbf{u}) = 0, \quad (25)$$

$$\frac{\partial}{\partial t}(\rho\mathbf{u}) + \nabla\cdot\left\{\rho\mathbf{u}\mathbf{u} + \left[P_{th} + \frac{B^2}{8\pi}\right]\mathbf{I} - \frac{\mathbf{B}\mathbf{B}}{4\pi}\right\} = -\mathbf{F}_{cr}, \quad (26)$$

$$\frac{\partial \epsilon}{\partial t} + \nabla\cdot\left\{\left[\epsilon + P_{th} + \frac{B^2}{8\pi}\right]\mathbf{u} - \frac{(\mathbf{u}\cdot\mathbf{B})\,\mathbf{B}}{4\pi} + \right. \\ \left. + \frac{c}{4\pi}(\mathbf{E}-\mathbf{E_0})\times\mathbf{B}\right\} = -\mathbf{u}_{cr}\cdot\mathbf{F}_{cr}, \quad (27)$$

$$\frac{\partial \mathbf{B}}{\partial t} + c\nabla\times\mathbf{E} = 0, \quad (28)$$

where $\mathbf{I}$ is the unitary dyadic tensor, $\epsilon = \rho u^2/2 + B^2/8\pi + P_{th}/(\gamma_{th}-1)$ is the total energy density with $\gamma_{th} = 5/3$ the adiabatic index of the thermal gas, $\mathbf{E}_0$ and $\mathbf{E}$ are the electric fields given by

$$\mathbf{E}_0 = -\frac{1}{c}\mathbf{u}\times\mathbf{B}, \quad (29)$$

$$\mathbf{E} = \mathbf{E}_0 - \frac{1}{c}\frac{n_{cr}}{n_e}(\mathbf{u}_{cr}-\mathbf{u})\times\mathbf{B}, \quad (30)$$

where $n_e = n_{cr} + n_i$ is as before the electrons number density, and $\mathbf{F}_{cr}$ is the force density felt by the CRs:

$$\mathbf{F}_{cr} = qn_{cr}\mathbf{E} + \frac{1}{c}\mathbf{J}_{cr}\times\mathbf{B}. \quad (31)$$

The orbits of the macro-particles are evolved using the the Lorentz force with the electromagnetic fields interpolated from the grid values:

$$\frac{d\mathbf{p}_j}{dt} = q\mathbf{E} + \frac{q}{c}\mathbf{v}_j\times\mathbf{B} \quad (32)$$

where $\mathbf{p}_j$ and $\mathbf{v}_j$ are the momentum and velocity of the particle j.

It should be pointed out that the electric field $\mathbf{E}$ (Eq. 30) differs from $\mathbf{E}_0$ by the inclusion of the CR Hall effect which is not taken into account in Eq. 8. However, the effects of this term (of the order of n_{cr}/n_i for $n_{cr} \ll n_i$) can be considered negligible if $\mathbf{u}_{cr} \sim \mathbf{u}$, which is the case for the transverse Alfvén modes we are interested in.

The above equations are solved in a periodic, cartesian, one-dimensional domain. The MHD equations are discretized using an conservative formulation, the fluxes are calculated using the HLLD solver (adapted from the ATHENA code, Stone et al. 2008) and linear interpolation. The particles are evolved using the relativistic Boris pusher (adapted from the SKELETON particle-in-cell codes, Decyk 1995, 2007) with a leap-frog scheme, and first-order weighting for the particles deposit on the grid. The full time integration (MHD + particles) is performed using Runge-Kutta of second order. We verified the second order convergence of our code implementation against several linear test problems, as MHD waves with cold and not-cold CR distributions (with different relative densities n_{cr}/n_i) and the non-resonant Bell instability.

4 RESULTS

4.1 Simulations parameters

The initial conditions of the performed simulations consist of homogeneous MHD fields with null-velocity and mean magnetic field parallel to the axis of the simulation grid, and a distribution of CRs with anisotropy A_0 (distribution $g(\mu)d\mu$ given by Eq. 10), superimposed by a flat spectrum of circularly polarized waves with magnetic field amplitude $|B_{k0}|$.

The momentum distribution of CRs has power-law index $\alpha = 2.8$, with $\gamma(p_{\rm min}) = 2$ and $p_{\rm max}/p_{\rm min} = 10$ (distribution $N(p)dp$ given by Eq. 19). We fix the ratio $v_A/c = 10^{-2}$. We vary the parameters A_0 and n_{cr}/n_i.

Tables 1 and 2 summarizes the parameters used for the simulations: n_{cr}/n_i, v_A/c, ratio between CR kinetic and magnetic energy density $\beta_{cr} \equiv W_{K,cr}/W_B$, ratio between thermal and magnetic pressures P_{th}/P_B, domain size L, grid resolution NX, number of particles per grid cell NP/NX, A_0, $(|B_{k0}|/B_0)^2$, polarization P, and total helicity σ_H.

The choice of parameters $(v_A/c, n_{cr}/n_i)$ is motivated by the conditions in the Galactic Halo and hot ionized medium, estimated in YL11. The high values of β_{cr} and A_0 (compared to the estimates by YL11) are chosen in order to maximize the growth rate of the fluctuations in the resonant energy interval, so that the waves amplified by the instability achieve higher amplitudes than the magnetic fluctuations (noise) caused by the limited number of macro-particles which sample the CR distribution function.

4.2 Linear phase of instability

Figures 1 and 2 show the dispersion relation extracted from the runs $d1$ and $d2$ ($A_0 = -0.3$, waves with polarization R and L, respectively). Each point in the figures is calculated by fitting the time-serie of one Fourier component of the magnetic field, between $t = 0$ and $t = t_{end}$ (all the points of the same color/style in each plot of Figures 1 and 2 are extracted from one single run). In this way we determine for each wavenumber k the phase, the phase speed, and the growth/damping rate. Figure 1 shows the growth/damping rate $\Gamma(k)$, while Figure 2 shows the real frequency $\omega_r(k)$ of the waves spectrum. The analytical solution from the dispersion relation (Eq. 14) is shown for comparison. The fitted values agree quite well with the theoretical values, except for large wavenumbers (inside the gray area), for which the numerical dissipation $\propto k^2$ dominates $\Gamma(k)$. Such agreement is observed also in the other runs, with the agreement in $\Gamma(k)$ better for the simulations with larger values of $|\Gamma_{\rm max}|$. For anisotropies smaller than $|A_0| = 0.1$ (and $v_A/c = 10^{-2}$, $n_{cr}/n_i = 10^{-4}$), for the same resolution and number of particles, the quality of the fitted values for $\Gamma(k)$ decays faster, due to the noise caused by the limited number of particles.

We present in the left column of Figure 3 the magnetic field power spectrum of models with different initial anisotropy $A_0 = +0.1, +0.2, +0.3$ (models $l1$-$l3$) at different times during the linear phase of the instability, when the distribution of particles is still almost identical to the initial one and the magnetic energy in the waves increase exponentially. The blue shaded region shows the wave numbers for which the growth rate (for waves with polarization L) is a power law with index related to the CR momentum distribution power-law index. The power spectrum in this region

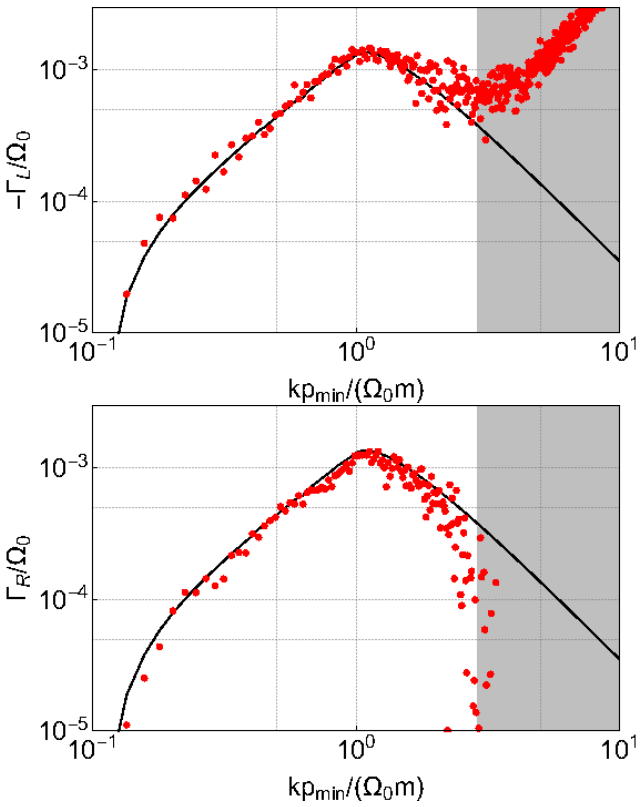

Figure 1. Wave growth/damping rate for models with initial anisotropy $A_0 = -0.3$ (models $d1$ and $d2$ in Table 2). *Upper plot:* damping rate of waves with polarization L. *Lower plot:* growth rate of waves with polarization R. The theoretical value given by Eq. 14 is shown for comparison (solid black line). The gray area comprehends the wavelengths $\leqslant 32$ grid cells, where the growth/damping rate is dominated by the numerical dissipation.

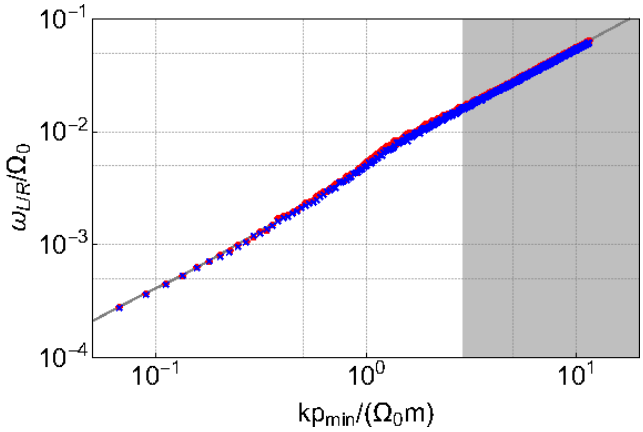

Figure 2. Real frequency of waves for models with initial anisotropy $A_0 = -0.3$ (models $d1$ and $d2$ in Table 2). *Red points:* waves with polarization L; *blue crosses:* waves with polarization R. The theoretical value given by Eq. 14 is shown for comparison (solid black line). The gray area comprehends the wavelengths $\leqslant 32$ grid cells, where the growth/damping rate is dominated by the numerical dissipation.

Table 1. Setup parameters for all the MHD-PIC simulations

v_A/c	P_{th}/P_B	$\gamma(p_{\rm min})$	$p_{\rm max}/p_{\rm min}$	α	$L\Omega_0/c$
10^{-2}	2	2	10	2.8	500

Table 2. Model parameters

run	A_0	n_{cr}/n_i	β_{cr}	$\lvert\Gamma_{\rm max}\rvert/\Omega_0$	$\lvert B_{k0}\rvert^2/B_0^2$	P	σ_H	$t_{end}\Omega_0$	NX	NP/NX
$d1$	-0.3	10^{-4}	5.2	1.4×10^{-3}	5×10^{-4}	$R(+1)$	$+1$	10^3	4096	4096
$d2$	-0.3	10^{-4}	5.2	1.4×10^{-3}	5×10^{-4}	$L(-1)$	-1	10^3	4096	4096
$l1$	$+0.1$	10^{-4}	5.2	3×10^{-4}	10^{-12}	$L(-1)$	0	2×10^3	4096	4096
$l2$	$+0.2$	10^{-4}	5.2	6×10^{-4}	10^{-12}	$L(-1)$	0	2×10^3	4096	4096
$l3$	$+0.3$	10^{-4}	5.2	9×10^{-4}	10^{-12}	$L(-1)$	0	2×10^3	4096	4096
$l4$	$+0.2$	2.5×10^{-5}	1.3	2×10^{-4}	10^{-12}	$L(-1)$	0	2×10^3	4096	4096
$l5$	$+0.2$	4×10^{-4}	20.8	2.4×10^{-3}	10^{-12}	$L(-1)$	0	2×10^3	4096	4096
$s1$	$+0.1$	10^{-4}	5.2	3×10^{-4}	2×10^{-12}	R, L	0	2×10^5	4096	1024
$s2$	0	10^{-4}	5.2	0	2×10^{-12}	R, L	0	2×10^5	4096	1024
$s3$	-0.1	10^{-4}	5.2	4×10^{-4}	2×10^{-12}	R, L	0	2×10^5	4096	1024
$s4$	-0.2	10^{-4}	5.2	8×10^{-4}	2×10^{-12}	R, L	0	2×10^5	4096	1024
$s5$	-0.3	10^{-4}	5.2	1.4×10^{-3}	2×10^{-12}	R, L	0	2×10^5	4096	1024
$s6$	0	10^{-4}	5.2	0	2×10^{-12}	R, L	0	10^5	4096	512
$s7$	0	10^{-4}	5.2	0	2×10^{-12}	R, L	0	10^5	4096	2048

increases in amplitude but keeping the slope during the measured times, this increase is faster for the higher absolute initial anisotropy. For wavenumbers smaller than those in the blue-shaded region, the amplitude remains nearly constant, as expected for the zero growth rate in this region.

Using this magnetic energy spectrum, we estimate the lower limit of the pitch-angle diffusion coefficient $\widetilde{D}^{QL}_{\mu\mu}(\delta t)$ provided by the quasilinear theory (Eq. A32 in Appendix):

$$\widetilde{D}^{QL}_{\mu\mu}(t,\mu,p,\delta t) \equiv \frac{\Omega^2(1-\mu^2)}{2}\int_0^\infty dk \frac{\overline{|\mathbf{B}(k,t)|^2}}{B_0^2}\times$$
$$\times\left\{[1+\overline{\sigma_H(k,t)}]\frac{\sin\left[(v\mu k+\Omega)\,\delta t\right]}{(v\mu k+\Omega)}+\right.$$
$$\left.+[1-\overline{\sigma_H(k,t)}]\frac{\sin\left[(v\mu k-\Omega)\,\delta t\right]}{(v\mu k-\Omega)}\right\}, \quad (33)$$

where the overbar means an average in time between $t-\delta t$ and t; here we neglect the real frequency of the waves $\omega_r(k)$ ($\ll\Omega$) in the resonance function. The helicity spectrum $\sigma_H(k,t)$ is calculated from the transverse electric field spectrum (Gary 1993):

$$\sigma_H(k,t) = -2\frac{k}{|k|}\frac{\mathrm{Im}\left\{E_y(k,t)E_z^*(k,t)\right\}}{|\mathbf{E}(k,t)|^2}. \quad (34)$$

We compare the quasilinear estimative with the directly measured diffusion coefficient

$$D_{\mu\mu}(t,\mu,p,\delta t) = \left\langle\frac{[\mu(t)-\mu(t-\delta t)]^2}{2\delta t}\right\rangle, \quad (35)$$

where $\mu(t-\delta t)$ and $\mu(t)$ are cosine of the pitch angle for the same particle at two consecutive times separated by δt (see for example Xu & Yan 2013; Weidl et al. 2015; Cohet & Marcowith 2016). The average $\langle\cdot\rangle$ is taken over all the particles in the simulation with momentum and pitch-angle cosine in a tiny interval $[p,p+\Delta p)$, $[\mu,\mu+\Delta\mu)$.

The distribution in momentum of the ratio $\langle D_{\mu\mu}(\delta t)/\widetilde{D}^{QL}_{\mu\mu}(\delta t)\rangle_\mu$ (averaged over all the values of μ, for $|\mu|\leqslant 0.95$) are shown in the right column of Figure 3, for the same models and times as for the energy spectra showed in the left column. We employ a time interval $\delta t\Omega_0 = 10^3$. For the fastest growing mode between these runs (model $l5$ in Table 2) we have $\delta t\Gamma_{\rm max}\approx 2.4$. For all models the ratio $\langle D_{\mu\mu}(\delta t)/\widetilde{D}_{\mu\mu}(\delta t)\rangle_\mu$ is very close to one.

Figure 4 is similar to Figure 3, but it shows a comparison between models with fixed anisotropy A_0 and different values of n_{cr}/n_i (models $l2$, $l4$, and $l5$ in Table 2). While the models with lower growth rate of the instability $|\Gamma_{\rm max}|$ (models $l2$ and $l4$) present the better agreement between $D_{\mu\mu}(\delta t)$ and $\widetilde{D}^{QL}_{\mu\mu}(\delta t)$, the model with higher n_{cr}/n_i (model $l5$) shows a diffusion rate $D_{\mu\mu}(\delta t)$ about two times larger than $\widetilde{D}^{QL}_{\mu\mu}(\delta t)$ for the final time.

4.3 Instability saturation

Figure 5 shows the time evolution of the CR pressure anisotropy and of the total magnetic energy of the waves (normalized by the energy of the mean field) for models $s1$-$s5$ starting with different anisotropies A_0 (see Table 2). It shows clearly the reduction of the absolute total anisotropy, although the values do not achieve zero by the end of our simulations. One control simulation with initial zero anisotropy (model $s2$) is shown to be stable and to continue isotropic until the end of the simulation. After $t\Omega_0\sim10^4$, the total magnetic energy in the fluctuations begins to saturate, at higher values for the models with higher $|A_0|$. The vertical lines in Figure 5 indicate the times in different regimes of the instability: $t\Omega_0 = 2\times10^3$ (*linear phase*), $t\Omega_0 = 2\times10^4$ (*beginning of the saturation phase*), and $t\Omega_0 = 10^5$ and $t\Omega_0 = 2\times10^5$ (*late times during the saturation phase*). We observe that the energy of the waves in the isotropic case also increases initially and saturates, caused by the numeri-

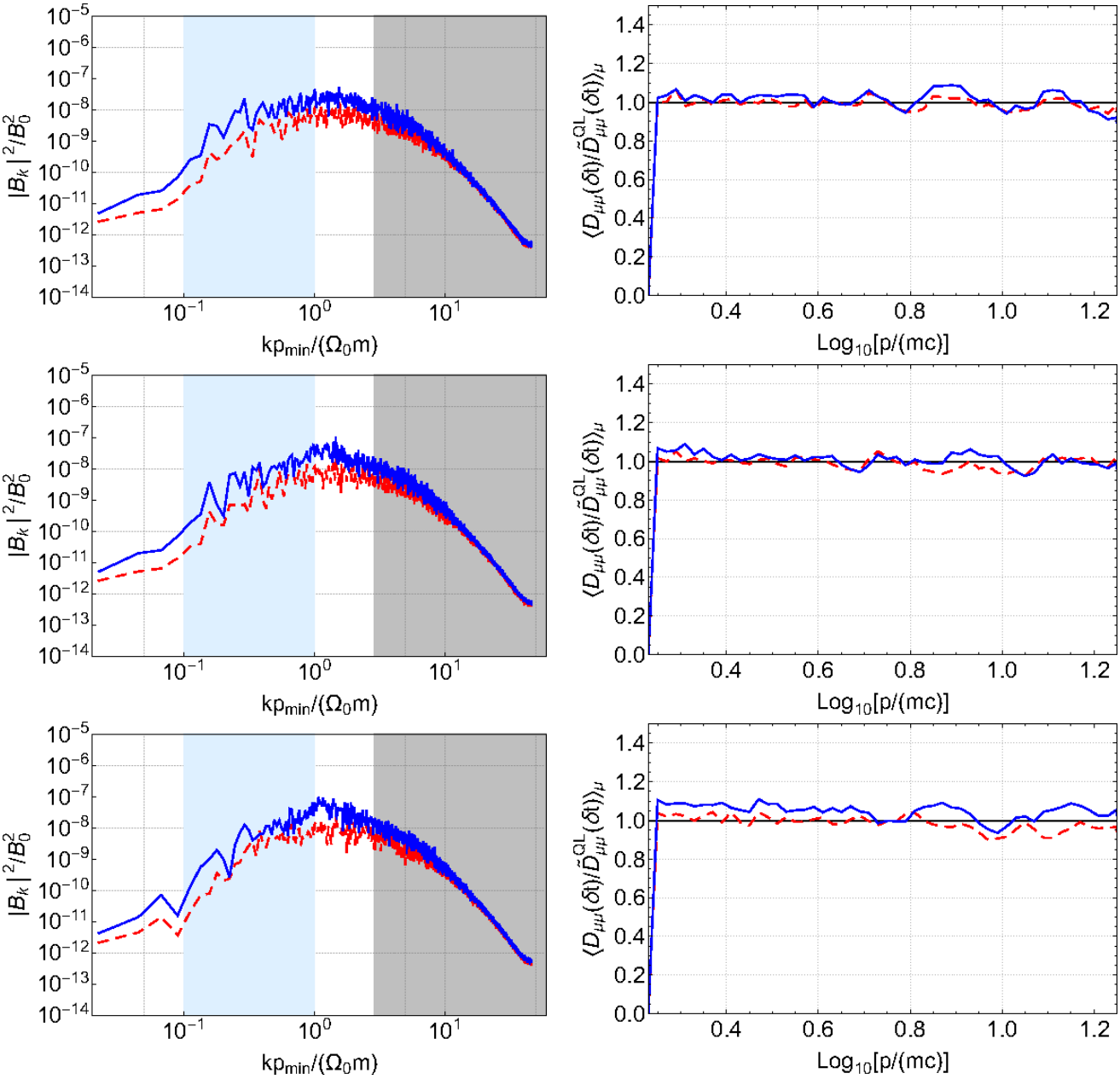

Figure 3. Normalized power spectrum of magnetic field $|B(k)|^2/B_0^2$ (*left column*) and $\langle D_{\mu\mu}(\delta t)/\widetilde{D}^{QL}_{\mu\mu}(\delta t)\rangle_\mu$ ratio (*right column*) for models starting with different anisotropies A_0: +0.1 (top row), +0.2 (middle row), +0.3 (lower row), corresponding to models *l*1-*l*3 in Table 2. Lines with different colors indicate different times: $t\Omega_0 = 10^3$ (red dashed line), $t\Omega_0 = 2\times10^3$ (blue solid line). In the power spectrum plots, the region where the numerical dissipation dominates are gray-shaded (wavelengths $\leqslant$ 32 grid cells); the blue shaded region represents the interval $\Omega_0 m_{cr}/p_{\rm max} < k < \Omega_0 m_{cr}/p_{\rm min}$.

cal noise due to the limited number of particles. This value is smaller for higher number of particles (see Figure 6 for a comparison between simulations with different NP/NX). It indicates the minimum limit in the instability growth rate that we can simulate (with fixed resolution), below which the properties are dominated by the numerical noise.

We show in Figure 7, the magnetic power spectrum, the ratio $\langle D_{\mu\mu}(\delta t)/\widetilde{D}^{QL}_{\mu\mu}(\delta t)\rangle_\mu$, and the anisotropy distribution in the momentum $A(p)$, for two different models ($A_0 = +0.1$ and $A_0 = -0.3$). We plot each quantity at the four times (indicated by different colors) of the different regimes described above (see also Figure 5). In the beginning of the saturation phase, the magnetic energy in the blue-shaded region is already saturated for the highest wave-numbers, but it is still growing for the smallest wave numbers.

The diffusion coefficients in Figure 7 are calculated using time intervals $\delta t\Omega_0 = 10^3$ ($\delta t\Gamma_{\rm max} \approx 1.4$ for model *s*5 which has the highest $\Gamma_{\rm max}$). During the linear phase, $D_{\mu\mu}(\delta t)$ compares well with $\widetilde{D}^{QL}_{\mu\mu}(\delta t)$. For the later times these values are still comparable by a factor of 3. The fluctuation is stronger for the higher initial anisotropy model $A_0 = +0.3$, at the beginning of the saturation phase ($t\Omega_0 =$

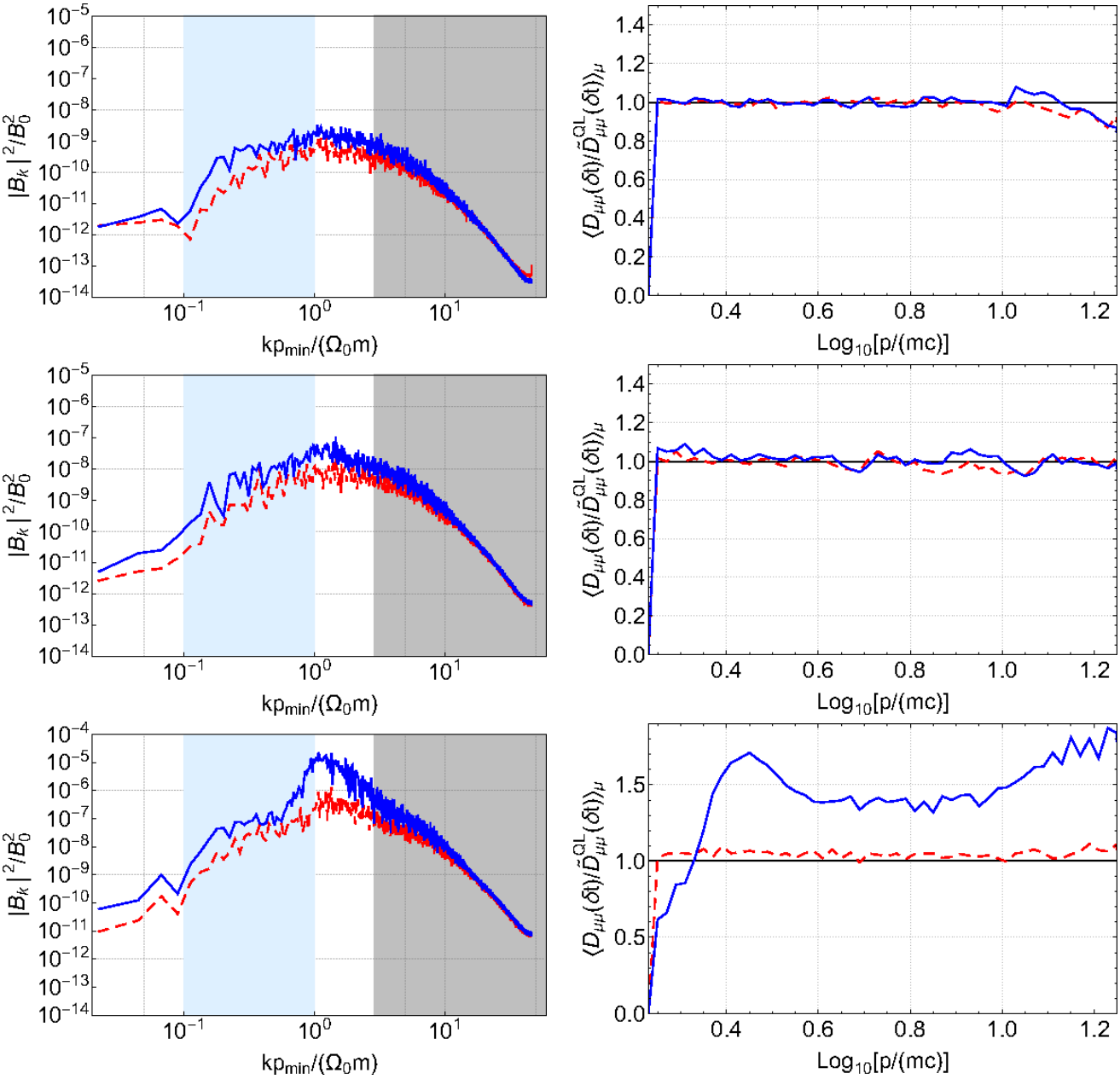

Figure 4. Same as Fig. 3, for models with different n_{cr}/n_i : 2.5×10^{-5} (*top row*), 10^{-4} (*middle row*), 4×10^{-4} (*lower row*), which correspond respectively to models $l4$, $l2$, and $l5$ of Table 2.

2×10^4, red dashed line in Figure 7), when the magnetic energy spectrum is more irregular inside the wavenumber interval of main resonance (blue area). This effect can be caused by the shortness of the time interval δt compared to the correlation time t_c of the rate of change of the pitch-angle (see Appendix A) for the particles of higher energies, as the deviation is larger for these particles.

For the initial linear phase the anisotropy distribution of both models is shown to be almost identical to the initial one. In the beginning of the saturation phase, however, the low-energy CRs (the bulk of the CRs distribution) are already almost totally isotropized (at the same time the instability growth drops for the corresponding resonant wavenumbers). The relatively strong fluctuations in A seen at $p \approx p_{\rm min}$ is an artifact caused by the discontinuity at $p = p_{\rm min}$ of the distribution function $f(p)$ employed (Eq. 19). These peaks disappear when we repeat the simulations extending $f(p)$ towards smaller p with a steep, growing power law (Figure 8). The single power law in the interval $[p_{\rm min}, p_{\rm max}]$, however, has the advantage of the simplicity in the analytical treatment. At the final time of the simulation, the CRs of the highest energies still preserve the initial anisotropy.

In Figure 9 we show the scattering rate $\nu_{scatt} \equiv \langle 2D_{\mu\mu}(\delta t)/(1-\mu^2)\rangle_\mu$ during the saturated phase (at the final time of the simulation) for three models $A_0 = -0.1, -0.2, -0.3$. The distribution as a function of the CR momentum is almost flat for the momentum range which

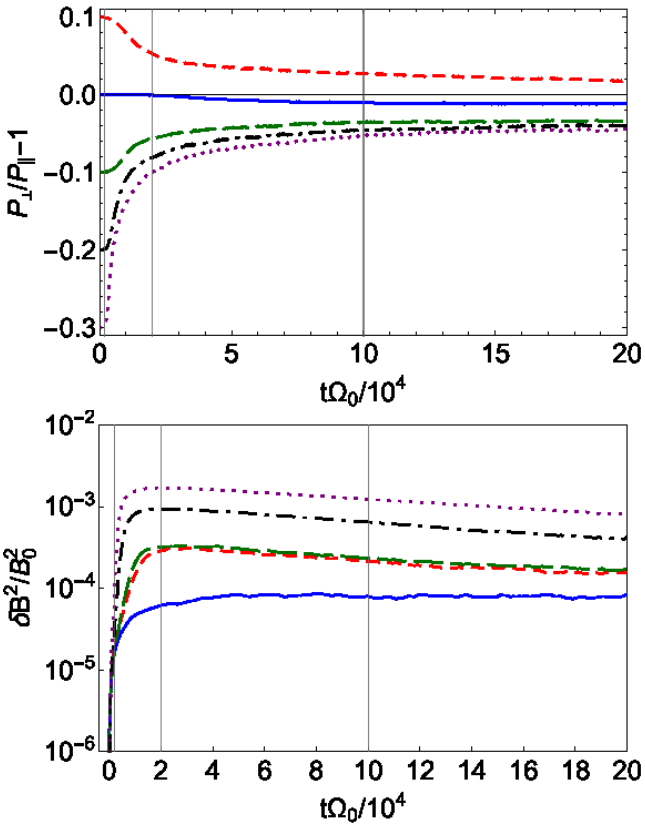

Figure 5. Time evolution of the total magnetic energy in fluctuations normalized by the energy in the mean field (upper panel) and CR total pressure anisotropy (bottom panel) for models starting with different initial anisotropies A_0 : +0.1 (red dashed line), 0 (blue solid line), −0.1 (green long-dashed line), −0.2 (black dot-dashed line), −0.3 (magenta dotted line), which correspond to models $s1$-$s5$ in Table 2. The vertical lines mark four different stages of the instability evolution: linear, early saturation, and late saturation times (from smaller to larger t).

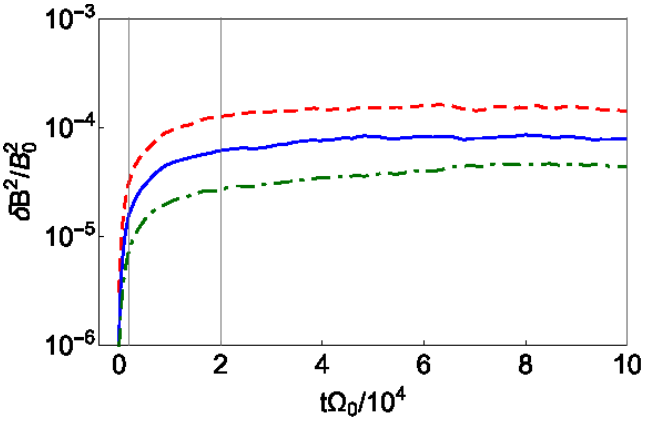

Figure 6. Time evolution of the total magnetic energy in fluctuations normalized by the energy in the mean field for models starting with initial anisotropies $A_0 = 0$ and different number of particles NP/NX: 512 (red dashed line), 1024 (blue solid line), 2048 (green dot-dashed line), which correspond respectively to models $s6$, $s2$, and $s7$ in Table 2.

is isotropized by this time, but decaying for larger energies. This is expected as the high-energy particles are resonant with waves which are still growing.

5 SUMMARY AND CONCLUSIONS

Using one-dimensional hybrid PIC-MHD simulations, we study numerically the evolution of the CR gyroresonance instability, triggered by a distribution of CR protons with initial anisotropy (with respect to the local mean magnetic field direction) in pressure ($P_{cr,\parallel} \neq P_{cr,\perp}$). We restricted our analysis to parallel-propagating modes, which are the fastest growing modes. During the linear phase of the instability the growth rate and phase speed of the modes with Right and Left circular polarization show excellent agreement with the theoretical dispersion relation, for both initial setups with $P_{cr,\parallel} > P_{cr,\perp}$ and $P_{cr,\parallel} < P_{cr,\perp}$.

In all our simulations the non-linear wave-particle effects are important. After a short initial period of exponential growth of the waves, the scattering and consequent isotropization of the CRs momentum distribution is the mechanism which gradually saturates the instability growth. The low-energy CRs are isotropized faster than those of the higher energies. The amplitude of the waves and the scattering rate of particles during the saturation phase are larger for initially larger maximum instability growth rate $\Gamma_{\rm max}$.

We extracted from the simulations the pitch angle diffusion coefficient $D_{\mu\mu}$ for the evolution of the CR distribution function averaged over a time-scale $\delta t \lesssim \Gamma_{\rm max}^{-1}$, and we find the empirical values in good agreement with the QLT estimates for static waves (within a factor of 3). This agreement is shown to be better for our simulations with smaller $\Gamma_{\rm max}$. Indeed, due to limitations imposed by the noise caused by the low sample of macro-particles in the PIC technique, all our simulations have parameters which produce a maximum growth rate of the instability much higher than expected in realistic situations. Nonetheless, this direct confirmation of the applicability of the QLT to estimate the CR scattering by the gyroresonance instability is a valuable support for theoretical models connecting the large-scale turbulence cascade with the "microphysics" of the CR instabilities (YL11), and for subgrid models in large-scale simulations involving CR transport (for example Everett & Zweibel 2011; Evoli & Yan 2014; del Valle, Romero, & Santos-Lima 2015; Pfrommer et al. 2017), as direct numerical simulations cannot cover the huge range of scales involved.

In conclusion, the outcome of this work provide a solid foundation for developing further investigations on the role of the CR gyroresonance instability on CR propagation. This includes for example the use of a setup where the pressure anisotropy is generated naturally by continuous compression or shear (e.g. Kunz, Schekochihin, & Stone 2014; Riquelme, Quataert, & Verscharen 2015; Sironi & Narayan 2015), the combined effect with the streaming instability generated by the presence of CR drift, and the use of three-dimensional simulations which would better represent the turbulence cascade from the instability generated waves, necessary for understanding the decaying of the instability and the effect of successive large-scale random compressions/expansions provided by the large-scale turbulence (Melville, Schekochihin, & Kunz 2016). As already stressed

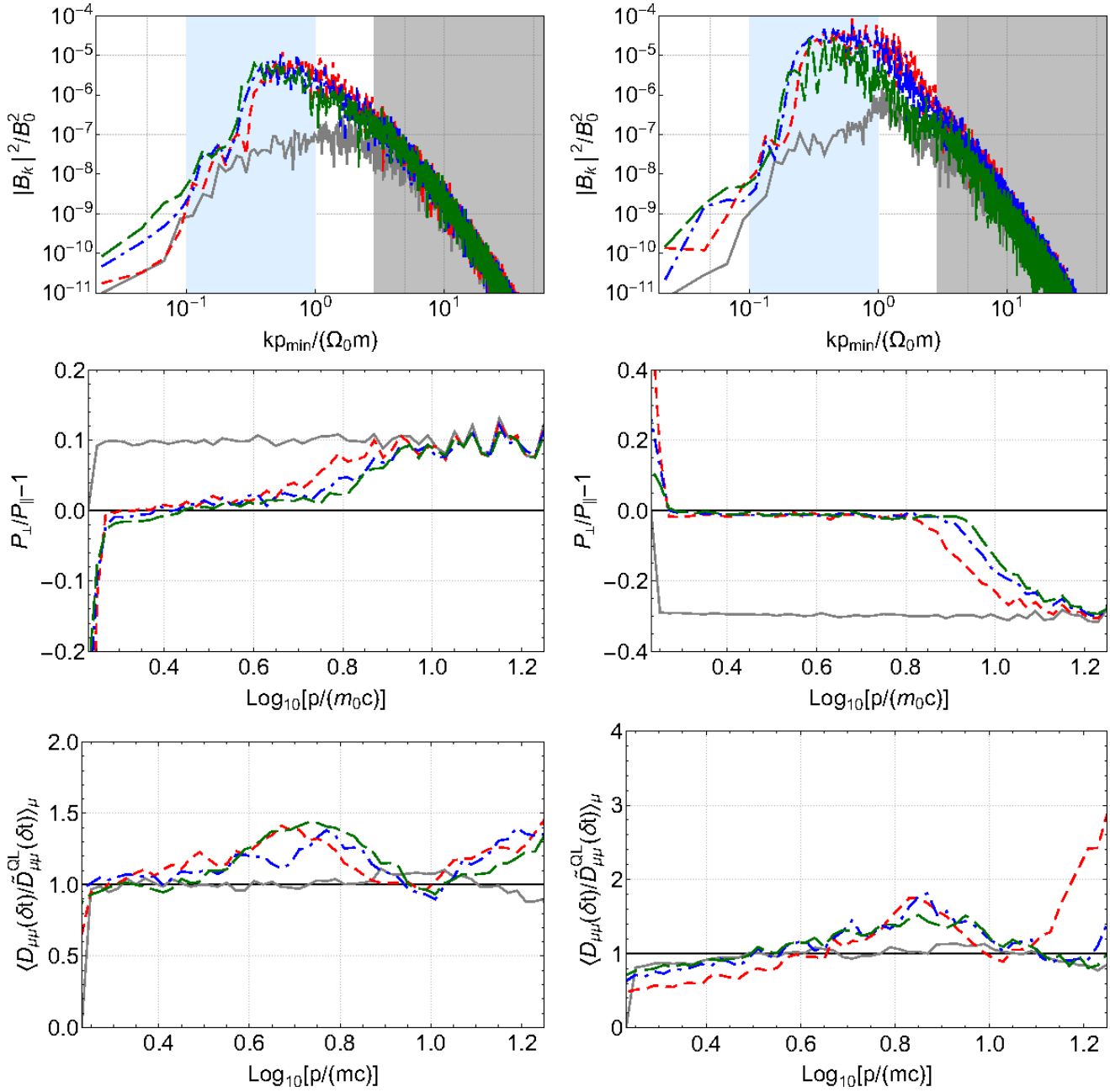

Figure 7. Normalized power spectrum of magnetic field $|B(k)|^2/B_0^2$ (upper row), $\langle D_{\mu\mu}(\delta t)/\widetilde{D}^{QL}_{\mu\mu}(\delta t)\rangle_\mu$ ratio (middle row), and distribution of CR pressure anisotropy A in momentum (bottom row) for models $s1$ and $s5$ (see Table 2) with different anisotropies A_0: $+0.1$ (left column) and -0.3 (right column). The lines with different colors indicate different times (shown in Figure 5): $t\Omega_0 = 2\times10^3$ (gray solid line), $t\Omega_0 = 2\times10^4$ (red dashed line), $t\Omega_0 = 10^5$ (blue dot-dashed line), $t\Omega_0 = 2\times10^5$ (green long-dashed line). In the power spectrum plots (upper row), the gray area indicates the wave number interval where numerical dissipation dominates (wavelengths $\leqslant 32$ grid cells); the blue area represents the wave number interval $\Omega_0 m_{cr}/p_{\max} < k < \Omega_0 m_{cr}/p_{\min}$.

before, the precise quantitative knowledge of the scattering provided by microscopic instabilities is an indispensable ingredient for building more realistic models for the CR propagation in the Galaxy and in the ICM, needed for our correct understanding and interpretation of almost all high-energy phenomena.

ACKNOWLEDGEMENTS

O.L. acknowledges the DESY Summer Student Programme 2016, during which part of this project was developed. R.S.L. acknowledges A. Beresnyak, E.M. de Gouveia Dal Pino, C.-S. Jao, Y. Mardoukhi, and M. Pohl for very useful comments and discussions; he is also indebted to M.V. del Valle and S. Vafin for their invaluable detailed suggestions. The authors would like to thank the anonymous referee who helped to improve this work with his/her comments and suggestions.

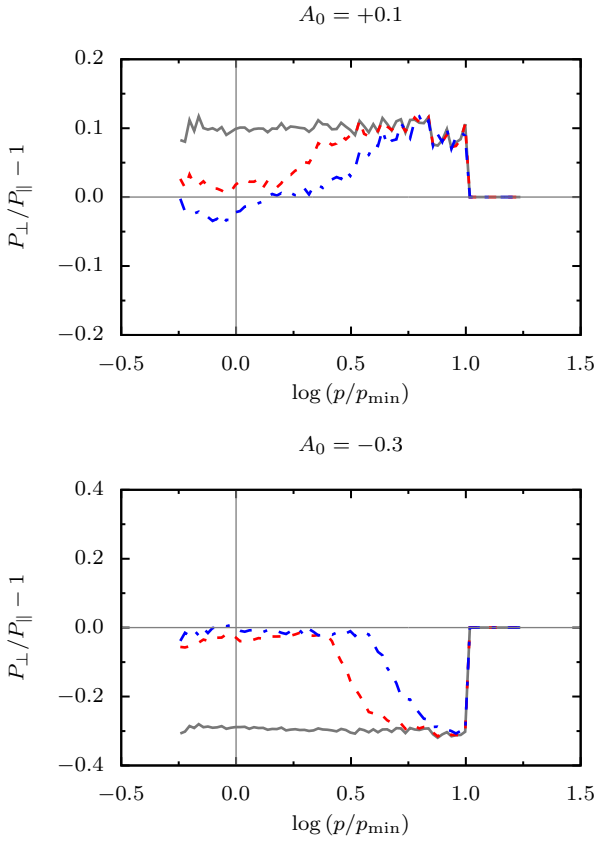

Figure 8. Distribution of the pressure anisotropy in momentum $A(p)$ for the modified models $s1$ (upper panel) and $s5$ (bottom panel). The modification consists in the extension of the CRs distribution, originally given by a single power-law ($\propto p^{-2.8}$) in the compact momentum interval $[p_{\rm min}, p_{\rm max}]$, to include the low momentum interval $[0.1p_{\rm min}, p_{\rm min}]$ where it assumes a steep, growing power-law ($\propto p^{5.6}$). The lines with different colors indicate different times: $t\Omega_0 = 2\times10^3$ (gray solid line), $t\Omega_0 = 2\times10^4$ (red dashed line), $t\Omega_0 = 10^5$ (blue dot-dashed line).

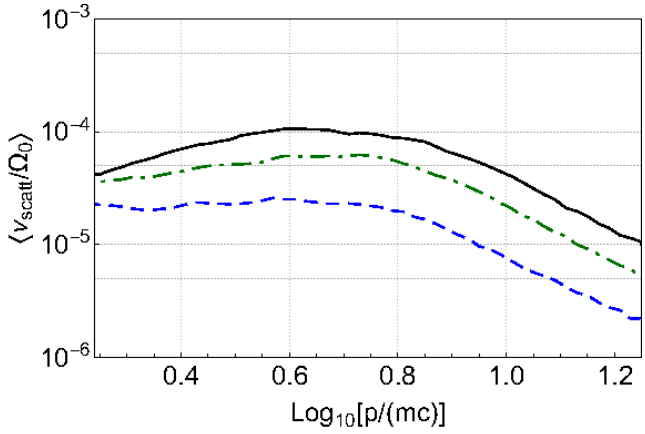

Figure 9. Distribution of the scattering rate $\nu_{scatt} = \langle 2D_{\mu\mu}(\delta t)/(1-\mu^2)\rangle_\mu$ (normalized by Ω_0) at time $t\Omega_0 = 2\times10^5$ (later time during the saturation phase, see last vertical line in Figure 5) for models with different initial anisotropy $A_0 = -0.1$ (blue dotted line), -0.2 (green dot-dashed line), -0.3 (black solid line), corresponding to models $s3$-$s5$ in Table 2.

REFERENCES

Achatz U., Steinacker J., Schlickeiser R., 1991, A&A, 250, 266
Amato E., Blasi P., 2009, MNRAS, 392, 1591
Bai X.-N., Caprioli D., Sironi L., Spitkovsky A., 2015, ApJ, 809, 55
Bell A. R., 2004, MNRAS, 353, 550
Bell A. R., Lucek S. G., 2001, MNRAS, 321, 433
Brose R., Telezhinsky I., Pohl M., 2016, A&A, 593, A20
Bykov A. M., Brandenburg A., Malkov M. A., Osipov S. M., 2013, SSRv, 178, 201
Caprioli D., Spitkovsky A., 2014, ApJ, 783, 91
Cohet R., Marcowith A., 2016, A&A, 588, A73
Decyk V. K., 2007, CoPhC, 177, 95
Decyk V. K., 1995, CoPhC, 87, 87
del Valle M. V., Romero G. E., Santos-Lima R., 2015, MNRAS, 448, 207
Di Sciascio G., Iuppa R., 2014, arXiv, arXiv:1407.2144
Everett J. E., Zweibel E. G., 2011, ApJ, 739, 60
Evoli C., Yan H., 2014, ApJ, 782, 36
Farmer A. J., Goldreich P., 2004, ApJ, 604, 671
Gary S. P., 1993, tspm.book, 193
Ginzburg V. L., 1966, SvA, 9, 877
Jokipii J. R., 1966, ApJ, 146, 480
Kunz M. W., Schekochihin A. A., Stone J. M., 2014, PhRvL, 112, 205003
Lazarian A., 2016, ApJ, 833, 131
Lazarian A., Beresnyak A., 2006, MNRAS, 373, 1195
Longair M. S., 2011, hea..book,
Lucek S. G., Bell A. R., 2000, MNRAS, 314, 65
Melville S., Schekochihin A. A., Kunz M. W., 2016, MNRAS, 459, 2701
Nava L., Gabici S., 2013, MNRAS, 429, 1643
Pfrommer C., Pakmor R., Schaal K., Simpson C. M., Springel V., 2017, MNRAS, 465, 4500
Riquelme M. A., Quataert E., Verscharen D., 2015, ApJ, 800, 27
Santos-Lima R., de Gouveia Dal Pino E. M., Kowal G., Falceta-Gonçalves D., Lazarian A., Nakwacki M. S., 2014, ApJ, 781, 84
Santos-Lima R., Yan H., de Gouveia Dal Pino E. M., Lazarian A., 2016, MNRAS, 460, 2492
Schekochihin A. A., Cowley S. C., 2006, PhPl, 13, 056501
Schekochihin A. A., Cowley S. C., Kulsrud R. M., Hammett G. W., Sharma P., 2005, ApJ, 629, 139
Schlickeiser R., 2002, cra..book,
Sironi L., Narayan R., 2015, ApJ, 800, 88
Skilling J., 1975, MNRAS, 172, 557
Skilling J., 1970, MNRAS, 147, 1
Skilling J., 1971, ApJ, 170, 265
Stix T. H., 1962, tpw..book,
Stone J. M., Gardiner T. A., Teuben P., Hawley J. F., Simon J. B., 2008, ApJS, 178, 137-177
Weidl M. S., Jenko F., Teaca B., Schlickeiser R., 2015, ApJ, 811, 8
Wentzel D. G., 1969, ApJ, 156, 303
Xu S., Yan H., 2013, ApJ, 779, 140
Yan H., 2015, ASSL, 407, 253
Yan H., Lazarian A., 2011, ApJ, 731, 35
Yan H., Lazarian A., 2008, ApJ, 673, 942-953
Yan H., Lazarian A., 2002, PhRvL, 89, 281102
Yan H., Lazarian A., Petrosian, V., 2008, ApJ, 684, 1461
Yan H., Lazarian A., Schlickeiser, 2012, ApJ, 745, 140
Zhang B., Yan H., 2011, ApJ, 726, 90

APPENDIX A: QUASILINEAR FOKKER-PLANCK PITCH-ANGLE DIFFUSION COEFFICIENT

Consider the operational definition of the pitch-angle diffusion coefficient convenient to analyse the particles simulation:

$$D_{\mu\mu}(\mathbf{X}(t_0),t_0)=\frac{\left\langle[\mu(t)-\mu(t_0)]^2\right\rangle}{2(t-t_0)}, \tag{A1}$$

where the angle brackets $\langle\cdot\rangle$ represent an ensemble over all the particles with coordinates $\mathbf{X}=(X,Y,Z,\mu,p,\psi)$ at time t_0, where (X,Y,Z) are the coordinates of the guiding center, and (p,μ,ψ) are the momentum, cosine of pitch-angle, and gyro-phase, respectively. In what follows, we provide the derivation of $D_{\mu\mu}$ for particles travelling in an homogeneous plasma superimposed by a spectrum of small amplitude transverse electromagnetic waves, with circular polarization and propagating parallel to the mean magnetic field. We also show that the above definition coincides — using similar hypotheses — with the $D_{\mu\mu}$ coefficient in the Fokker-Planck equation for the evolution of the (ensemble) averaged distribution function derived through the quasilinear theory (see e.g. Achatz, Steinacker, & Schlickeiser 1991; Schlickeiser 2002).

Without loss of generality, we take $t_0=0$ from here:

$$\begin{aligned}D_{\mu\mu}&=\frac{\left\langle[\mu(t)-\mu(0)]^2\right\rangle}{2t}\\&=\frac{1}{2t}\left\langle\int_0^t ds\dot{\mu}'(s)\int_0^t d\xi\dot{\mu}'(\xi)\right\rangle\\&=\frac{1}{2t}\int_0^t ds\int_{-s}^{t-s}d\tau\left\langle\dot{\mu}'(s)\dot{\mu}'(s+\tau)\right\rangle,\end{aligned} \tag{A2}$$

where the prime means the integration is to be performed along the unperturbed particles orbit coordinates $\mathbf{X}'$. Adopting a cartesian coordinate frame with the $x-$axis pointing in the direction of the mean magnetic field $\mathbf{B_0}$,

$$\begin{aligned}X'&=X+v\mu s,\\Y'&=Y,\\Z'&=Z,\\p'&=p,\\\mu'&=\mu,\\\psi'&=\psi-\varepsilon\Omega s,\end{aligned} \tag{A3}$$

where $v=p/\gamma m$ is the particle speed, $\gamma=\left(1-v^2/c^2\right)^{-1/2}$, c is the light speed, m is the rest mass of the particles, $\varepsilon=q/|q|$ is the signal of the particles charge, and $\Omega=|q|B_0/\gamma mc$ is the particles cyclotron frequency (the unprimed phase-space coordinates are to be understood at time $t=0$).

Assuming the existence of a correlation time t_c so that the correlation $\langle\dot{\mu}'(s)\dot{\mu}'(s+\tau)\rangle$ decays fast for $|\tau|>t_c$, then the main contribution to the integral A2 comes from the interval $-t_c\leqslant\tau\leqslant t_c$. For $t\gg t_c$, the intervals of the second integral can be replaced by $-t$ to t:

$$\begin{aligned}D_{\mu\mu}&\approx\frac{1}{2t}\int_0^t ds\int_{-t}^t d\tau\left\langle\dot{\mu}'(s)\dot{\mu}'(s+\tau)\right\rangle\quad(t\gg t_c)\\&\approx\frac{1}{t}\int_0^t ds\int_0^t d\tau\left\langle\dot{\mu}'(s)\dot{\mu}'(s+\tau)\right\rangle,\end{aligned} \tag{A4}$$

where in the last approximation we assumed the dependence of the correlation in τ to be approximately symmetric around zero.

Additionally, if the correlation $\langle\dot{\mu}'(s)\dot{\mu}'(s+\tau)\rangle$ does not depend on s, or if it changes on a time scale $t^*\gg t$,

$$D_{\mu\mu}\approx\int_0^t d\tau\left\langle\dot{\mu}'(0)\dot{\mu}'(\tau)\right\rangle. \tag{A5}$$

which coincides with the expression obtained from the quasilinear theory. In the remaining of this Appendix, we work out one expression for $D_{\mu\mu}$ in terms of the waves spectrum description.

Writing the transverse magnetic fluctuations in wave components with Left (L) or Right (R) circular polarization:

$$\begin{aligned}\delta B_y(x,t)&=\sum_n\int_{-\infty}^{\infty}dk\delta B_{y,n}(k,x,t)\\&=\sum_n\int_{-\infty}^{\infty}dk\frac{1}{2}\left[\delta A_n^L(k,x,t)+\delta A_n^R(k,x,t)\right]\end{aligned} \tag{A6}$$

$$\begin{aligned}\delta B_z(x,t)&=\sum_n\int_{-\infty}^{\infty}dk\delta B_{z,n}(k,x,t)\\&=\sum_n\int_{-\infty}^{\infty}dk\frac{i}{2}\,\mathrm{sign}(l_nk)\left[-\delta A_n^L(k,x,t)+\delta A_n^R(k,x,t)\right]\end{aligned} \tag{A7}$$

where l_n is the direction of propagation of the wave, $n=b,f$ are waves propagating backward ($n=b$, $l_n=-1$) and forward ($n=f$, $l_n=1$) to the mean magnetic field direction. The components δA_n^α ($\alpha=L,R$) are monocromatic waves given by

$$\begin{aligned}\delta A_n^\alpha(k,x,t)&=A_n^\alpha(k,t)\exp\left\{i\left[kx-\omega_{r,n}^\alpha(k)t\right]\right\}\\&=|A_n^\alpha(k,t)|\exp\left[i\phi_n^\alpha(k)\right]\exp\left\{i\left[kx-\omega_{r,n}^\alpha(k)t\right]\right\},\end{aligned} \tag{A8}$$

with

$$|A_n^\alpha(k,t)|=|A_n^\alpha(k,0)|\exp\left[\Gamma_n^\alpha(k)t\right] \tag{A9}$$

the absolute amplitude of the wave, and $\omega_{r,n}^\alpha,\Gamma_n^\alpha$ are the real frequency and growth/damping rate:

$$\omega_n^\alpha(k)=\omega_{r,n}^\alpha(k)+i\Gamma_n^\alpha(k), \tag{A10}$$

with $\omega_{r,n}^\alpha(-k)=-\omega_{r,n}^\alpha(k)$ and $\Gamma_n^\alpha(-k)=\Gamma_n^\alpha(k)$. Because the magnetic field is real, $\phi_n^\alpha(-k)=-\phi_n^\alpha(k)$ and $\delta A_n^\alpha(-k,x,t)=\delta A_n^{\alpha*}(k,x,t)$.

Assuming the waves have random phases,

$$\left\langle A_n^\alpha(k)A_m^{\beta*}(k')\right\rangle=|A_n^\alpha(k)|^2\delta_{nm}\delta_{\alpha\beta}\delta(k-k'), \tag{A11}$$

where the brackets here $\langle\cdot\rangle$ indicate average on an ensemble of realizations. From the Maxwell-Faraday equation relating the electromagnetic fields of the transverse waves

$$\frac{\partial\mathbf{B}}{\partial t}=-c\nabla\times\mathbf{E}, \tag{A12}$$

we can express the electric field in terms of the waves A_n^α:

$$\begin{aligned}\delta E_y(x,t)&=\sum_n\int_{-\infty}^{\infty}dk\delta E_{y,n}(k,x,t)\\&=-\sum_n\int_{-\infty}^{\infty}dk\frac{i}{kc}\frac{\partial}{\partial t}\delta B_{z,n}(k,x,t)\\&=-\sum_n\int_{-\infty}^{\infty}dk\frac{i}{2}\,\mathrm{sign}(l_nk)\left[-\frac{\omega_n^L(k)}{kc}\delta A_n^L(k,x,t)+\right.\\&\quad\left.+\frac{\omega_n^R(k)}{kc}\delta A_n^R(k,x,t)\right],\end{aligned}$$

(A13)

$$\begin{aligned}\delta E_z(x,t) &= \sum_n \int_{-\infty}^{\infty} dk \delta E_{z,n}(k,x,t) \\ &= \sum_n \int_{-\infty}^{\infty} dk \frac{i}{kc}\frac{\partial}{\partial t}\delta B_{y,n}(k,x,t) \\ &= \sum_n \int_{-\infty}^{\infty} dk \frac{1}{2}\left[\frac{\omega_n^L(k)}{kc}\delta A_n^L(k,x,t) + \right. \\ &\quad \left. + \frac{\omega_n^R(k)}{kc}\delta A_n^R(k,x,t)\right].\end{aligned} \tag{A14}$$

Now from the Lorentz force on the particle

$$\dot{\mathbf{p}} = \varepsilon e\left[\delta\mathbf{E} + \frac{1}{c}\mathbf{v}\times(\mathbf{B_0}+\delta\mathbf{B})\right], \tag{A15}$$

it is straightforward to show that

$$\begin{aligned}\dot{\mu} = \varepsilon\frac{\Omega}{B_0}\sqrt{1-\mu^2}\times \\ \times\left[\left(\delta B_z - \frac{c\mu}{v}\delta E_y\right)\cos\psi - \left(\delta B_y + \frac{c\mu}{v}\delta E_z\right)\sin\psi\right].\end{aligned} \tag{A16}$$

In the environments we are interested in, the phase-speed of the waves $\omega_{n,r}^{\alpha}/k \approx v_A \ll c$. Therefore we neglect the contribution of the electric field in A16:

$$\begin{aligned}\dot{\mu} = \varepsilon\frac{\Omega}{2B_0}\sqrt{1-\mu^2}\times \\ \times\left\{\delta B_z\left[\exp(i\psi)+\exp(-i\psi)\right] + \delta B_y i\left[\exp(i\psi)-\exp(-i\psi)\right]\right\}.\end{aligned} \tag{A17}$$

Using A17 in combination with A3, A6, and A7:

$$\begin{aligned}\left\langle\dot{\mu}'(s)\dot{\mu}'(s+\tau)\right\rangle = \frac{\Omega^2}{2B_0^2}\left(1-\mu^2\right)\sum_n\int_0^{\infty} dk\times \\ \times\Re\left\{|A_n^L(k,s)|^2\exp\left\{-i\left[kv\mu-\omega_n^{L*}(k)+\mathrm{sign}(l_n)\varepsilon\Omega\right]\tau\right\} + \right. \\ \left. + |A_n^R(k,s)|^2\exp\left\{-i\left[kv\mu-\omega_n^{R*}(k)-\mathrm{sign}(l_n)\varepsilon\Omega\right]\tau\right\}\right\}.\end{aligned} \tag{A18}$$

Then integrating A18,

$$\begin{aligned}\int_0^t d\tau\left\langle\dot{\mu}'(s)\dot{\mu}'(s+\tau)\right\rangle = \frac{\Omega^2}{2B_0^2}\left(1-\mu^2\right)\sum_n\int_0^{\infty} dk\times \\ \times\left\{|A_n^L(k,s)|^2\mathcal{R}(n,L,k,t) + |A_n^R(k,s)|^2\mathcal{R}(n,R,k,t)\right\}\end{aligned} \tag{A19}$$

where the resonance function $\mathcal{R}$ (Schlickeiser 2002; Weidl et al. 2015) is defined by:

$$\begin{aligned}\mathcal{R}(n,\alpha,k,t) \equiv \Re\left\{\frac{1-\exp\left[\Gamma_n^{\alpha}(k)t\right]\exp\left[-i\vartheta_n^{\alpha}(k)t\right]}{\left[-\Gamma_n^{\alpha}(k)+i\vartheta_n^{\alpha}(k)\right]}\right\} \\ = \frac{-\Gamma_n^{\alpha}\left[1-\exp\left(\Gamma_n^{\alpha}t\right)\cos\left(\vartheta_n^{\alpha}t\right)\right] + \vartheta_n^{\alpha}\exp\left(\Gamma_n^{\alpha}t\right)\sin\left(\vartheta_n^{\alpha}t\right)}{\left(\Gamma_n^{\alpha}\right)^2+\left(\vartheta_n^{\alpha}\right)^2},\end{aligned} \tag{A20}$$

where

$$\vartheta_n^{\alpha}(k) \equiv kv\mu - \omega_{r,n}^{\alpha}(k) - P(\alpha)\,\mathrm{sign}(l_n)\varepsilon\Omega, \tag{A21}$$

and $P(\alpha)$ is the polarization (-1 for $\alpha = L$ and $+1$ for $\alpha = R$).

For constant amplitude waves ($\Gamma_n^{\alpha}(k)\to 0$),

$$\lim_{\Gamma\to 0}\mathcal{R}(n,\alpha,k,t) = \frac{\sin\left[\vartheta_n^{\alpha}(k)t\right]}{\vartheta_n^{\alpha}(k)}, \tag{A22}$$

and the main contribution to the integral comes from $|\vartheta_n^{\alpha}(k)t| \leqslant \pi$. In the limit $t\to\infty$,

$$\lim_{t\to\infty}\left\{\lim_{\Gamma\to 0}\mathcal{R}(n,\alpha,k,t)\right\} = \pi\delta\left[\vartheta_n^{\alpha}(k)\right]. \tag{A23}$$

For finite $\Gamma_n^{\alpha}(k) < 0$ (damped waves),

$$\lim_{t\to\infty}\mathcal{R}(n,\alpha,k,t) = \frac{-\Gamma_n^{\alpha}(k)}{\left[\Gamma_n^{\alpha}(k)\right]^2+\left[\vartheta_n^{\alpha}(k)\right]^2} \quad (\Gamma_n^{\alpha}(k)<0), \tag{A24}$$

from which the limit $\Gamma\to 0$ gives again

$$\lim_{\Gamma\to 0^-}\left\{\lim_{t\to\infty}\mathcal{R}(n,\alpha,k,t)\right\} = \pi\delta\left[\vartheta_n^{\alpha}(k)\right]. \tag{A25}$$

We are interested in evaluating the diffusion during time intervals short compared to the growth/damping time of the wave, so that $|\Gamma_n^{\alpha}(k)t| \ll 1$. Keeping only first order terms in $\Gamma_n^{\alpha}(k)t$,

$$\begin{aligned}\mathcal{R}(n,\alpha,k,t) = \\ = \frac{\left(\Gamma_n^{\alpha}\right)^2 t\cos\left(\vartheta_n^{\alpha}t\right) + \vartheta_n^{\alpha}\left(1+\Gamma_n^{\alpha}t\right)\sin\left(\vartheta_n^{\alpha}t\right)}{\left(\Gamma_n^{\alpha}\right)^2+\left(\vartheta_n^{\alpha}\right)^2} + \mathcal{O}\left\{\left(\Gamma_n^{\alpha}t\right)^2\right\}\end{aligned} \tag{A26}$$

For the wavenumbers where $|\vartheta_n^{\alpha}(k)t| > |\Gamma_n^{\alpha}(k)t|$,

$$\begin{aligned}\mathcal{R}(n,\alpha,k,t) = \left(1+\Gamma_n^{\alpha}t\right)\frac{\sin\left[\vartheta_n^{\alpha}t\right]}{\vartheta_n^{\alpha}} + \\ + \mathcal{O}\left\{\left(\Gamma_n^{\alpha}/\vartheta_n^{\alpha}\right)^2\right\} + \mathcal{O}\left\{\left(\Gamma_n^{\alpha}t\right)^2\right\}.\end{aligned} \tag{A27}$$

Keeping t fixed, the above expression shows the main contribution of the resonance function $\mathcal{R}$ in the integral A19 comes from the wavenumbers with $|\vartheta_n^{\alpha}(k)t| \leqslant \pi$. Neglecting the term $\omega_{r,n}^{\alpha}(k)$ in the expression for $\vartheta_n^{\alpha}(k)$ (Eq. A21), it gives the following relative window in wave-numbers:

$$\frac{\Delta k}{|k_{\mathrm{res}}|} = \frac{2\pi}{\Omega t} = \gamma\frac{2\pi}{\Omega_0 t}, \tag{A28}$$

where $\vartheta_n^{\alpha}(k_{\mathrm{res}}) = 0$, and Ω_0 is the non-relativistic cyclo-frequency.

Assuming the fixed t is long enough so that $\Delta k/|k_{\mathrm{res}}| \ll 1$, we can approximate $\Gamma_n^{\alpha}(k) \approx \Gamma_n^{\alpha}(k_{\mathrm{res}})$ inside the resonance window. Using the notation $c = \Gamma_n^{\alpha}(k_{\mathrm{res}})t$, $x = \vartheta_n^{\alpha}t$, Eq. A26 becomes:

$$\mathcal{R}(n,\alpha,k,t) = t\left\{\frac{c^2\cos x + x(1+c)\sin x}{c^2+x^2}\right\}. \tag{A29}$$

Figure A1 shows the behaviour of $\mathcal{R}/t$ in the interval $-\pi \leqslant x \leqslant \pi$ for different values of c ($-0.5 \leqslant c \leqslant 0.5$). Therefore, for growing waves ($\Gamma_n^{\alpha} > 0$),

$$\mathcal{R}(n,\alpha,k,t) \geqslant \frac{\sin\left[\vartheta_n^{\alpha}(k)t\right]}{\vartheta_n^{\alpha}(k)}. \tag{A30}$$

Now returning to Eq. A19 and using the notation

$$\overline{|A_n^{\alpha}(k,t)|^2} \equiv \frac{1}{t}\int_0^t ds|A_n^{\alpha}(k,s)|^2, \tag{A31}$$

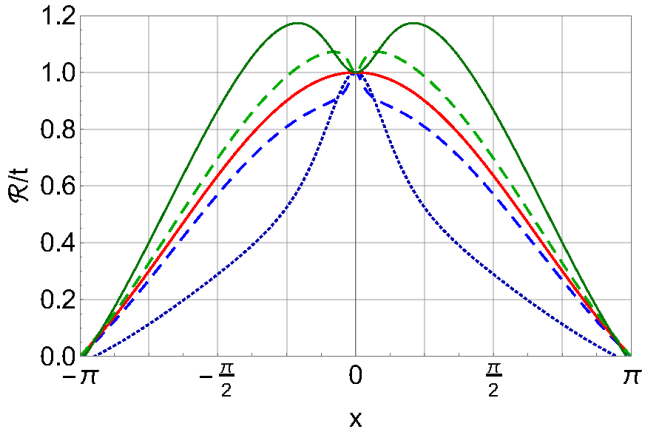

Figure A1. The plot of the $\mathcal{R}/t$ defined by Eq. A29 depending on x. The values of c is taken to be (from the lower to the upper curve) -0.5 (dotted dark blue), -0.1 (dashed blue), 0 (solid red), 0.1 (dashed green), and 0.5 (dotted dark green).

and

$$\widetilde{D}_{\mu\mu}(t) = \frac{\Omega^2}{2B_0^2}\left(1-\mu^2\right)\sum_{n,\alpha}\int_0^\infty dk\overline{|A_n^\alpha(k,t)|^2}\frac{\sin\left[\vartheta_n^\alpha(k)t\right]}{\vartheta_n^\alpha(k)}, \tag{A32}$$

we obtain (for growing waves):

$$D_{\mu\mu}(t) \geqslant \widetilde{D}_{\mu\mu}(t). \tag{A33}$$

This paper has been typeset from a TEX/LATEX file prepared by the author.